






ARTICLE

DOI: 10.1038/s41467-018-05575-w

OPEN

Ba₃Mg₃(BO₃)₃F₃ polymorphs with reversible phase transition and high performances as ultraviolet nonlinear optical materials

Miriding Mutailipu ^{1,2}, Min Zhang ¹, Hongping Wu¹, Zihua Yang ¹, Yihan Shen³, Junliang Sun ³ & Shilie Pan ¹

Nonlinear optical (NLO) materials are the vital components of future photoelectric technologies as they can broaden the tunable wavelength range supplied by common laser sources. However, the necessary prerequisites for a practical NLO material are rather strict. Accordingly, considerable efforts have been focused on finding potential NLO materials. Here we report two asymmetric beryllium-free borates *Pna*2₁- and *P6̄2m*-Ba₃Mg₃(BO₃)₃F₃ featuring NLO-favorable ²_∞[Mg₃O₂F₃(BO₃)₂] layered structures. The reversible phase transition among two polymorphs was demonstrated by multiple experimental tests. The optical measurements reveal that *Pna*2₁-Ba₃Mg₃(BO₃)₃F₃ possesses the optical properties required for ultraviolet NLO applications. Remarkably, *Pna*2₁-Ba₃Mg₃(BO₃)₃F₃ has a large laser damage threshold, a deep-ultraviolet cutoff edge, a favorable anisotropic thermal expansion as well as the capacity of insolubility in water. These optical properties can be comparable or superior to that of commercial NLO material β-BaB₂O₄, which make *Pna*2₁-Ba₃Mg₃(BO₃)₃F₃ a promising ultraviolet NLO material.

¹CAS Key Laboratory of Functional Materials and Devices for Special Environments, Xinjiang Technical Institute of Physics & Chemistry, CAS, Xinjiang Key Laboratory of Electronic Information Materials and Devices, 40-1 South Beijing Road, Urumqi 830011, China. ²University of Chinese Academy of Sciences, Beijing 100049, China. ³College of Chemistry and Molecular Engineering, Peking University, Beijing 100871, China. These authors contributed equally: Miriding Mutailipu, Min Zhang. Correspondence and requests for materials should be addressed to J.S. (email: junliang.sun@pku.edu.cn) or to S.P. (email: slpan@ms.xjb.ac.cn)

Nonlinear optical (NLO) materials applied from ultraviolet (UV) to infrared spectral ranges are the vital components of future photoelectric technologies^{1–4}. Accordingly, considerable and sustained efforts have been focused on designing and synthesizing new potential NLO materials^{5–9}. Generally speaking, a practical UV NLO material should simultaneously satisfy the following criteria: a noncentrosymmetric structure; a broad transparent spectral range down to the UV region ($\lambda < 400$ nm); a relatively large second-order nonlinear coefficient ($d_{ij} > 0.39$ pm/V); a moderate birefringence to satisfy the phase-matching condition, chemical stability (non-deliquescent), and resistance to laser (large laser damage threshold, large LDT); and ease of growth of large single crystals with high optical quality¹⁰. Targeting above conditions, until now, the borate system plays a dominant role in UV NLO materials because borates possess wide optical transparency windows, varied acentric structure types, high LDTs, and large polarizabilities^{11–18}. Therefore, a variety of commercial borate-based UV NLO materials have been widely investigated and developed. Among them, borates with planar $[\text{BO}_3]^{3-}$ anionic groups have always been at the center of the search for NLO materials with large second-harmonic generation (SHG) response and birefringence, which mainly benefits from the π -conjugated molecular orbitals of $[\text{BO}_3]^{3-}$ units^{19–22}. Based on this, several borates with $[\text{BO}_3]^{3-}$ NLO-active units in coplanar and aligned configuration were continuously reported with good optical properties, including $\text{KBe}_2\text{BO}_3\text{F}_2$ (KBBF)¹⁹, $\text{BaAlBO}_3\text{F}_2$ ²⁰, $\text{NaSr}_3\text{Be}_3\text{B}_3\text{O}_9\text{F}_4$ ²¹, $\text{Li Sr}(\text{BO})$ ²², etc.

For the sake of finding new novel UV or even deep-UV ($\lambda < 200$ nm) NLO crystals, an effective design tactic is to introduce fluorine into the structural framing of borate system based on the following considerations. First, the fluorine with the largest electronegativity ($\chi = 3.98$) can widen the transparency area and make the cutoff edge of borates blue-shift into UV or even deep-UV spectral region^{19–21,23–25}. Second, substituting oxygen with fluorine in $[\text{BO}_4]^{5-}$ maternal blocks to form $[\text{BO}_x\text{F}_{4-x}]^{(x+1)-}$ ($x = 0, 1, 2, 3$) fundamental building blocks can make the anionic groups more flexible, and the negative effective charges at the terminal oxygen will be partly reduced, resulting in a suitable SHG coefficient and birefringence^{26–29}. Third, the introduction of fluoride-containing flux can effectively decrease the viscosity of the borate systems during the growth of single crystals, which is a desirable choice for growing the large single crystals^{20,24,25,30}.

For us, besides selecting the appropriate system (borate) and introducing anion (fluorine), how to effectively design UV NLO materials with presupposed structures and properties is also critically important. The following ideas were considered for designing the target molecules: first, in order to manipulate the B–O fundamental building blocks into isolated planar $[\text{BO}_3]^{3-}$ configuration, we adjusted the ratio of cations and boron to >1.0 based on the rules proposed by Becker³¹. Second, we use the strategy of chemical cosubstitution to make structural modifications based on the classic NLO materials with the goal of obtaining new molecular structures contain NLO-favorable layered structures^{32,33}.

Motivated by these, considering that *s*-block elements Be and Mg, Sr and Ba appear tightly clustered in the periodic table with the similar electronic configurations, sharing many common physicochemical properties. Therefore, we attempted to substitute the Be and Sr atoms of $\text{Sr}_2\text{Be}_2\text{B}_2\text{O}_7$ (SBBO)¹ with Mg and Ba atoms through chemical cosubstitution idea to create new SBBO-like borates, which leads us to discover two new beryllium-free borates, *Pna*2₁- and *P62m*- $\text{Ba}_3\text{Mg}_3(\text{BO}_3)_3\text{F}_3$ (*Pna*2₁- and *P62m*-BMBF), featuring SBBO-like layered structures without structural instability. The $2_{\infty}[\text{Mg}_3\text{O}_2\text{F}_3(\text{BO}_3)_2]$ layers in both of them not only preserve the NLO-favorable structural habits of SBBO, but also introduce the Mg–F bonds served between layers as bridges

to enhance the interlayer interaction. Based on the top designing molecule structures, large-size single crystals of *Pna*2₁-BMBF were also grown through finding the suitable flux system. The optical measurements based on the crystal reveal that *Pna*2₁-BMBF possesses the NLO properties required for the UV NLO applications, which indicates that *Pna*2₁-BMBF is a potential UV NLO material.

Results

The reversible phase transition between two polymorphs.

Single crystal X-ray diffraction reveals that two new borates crystallize into the asymmetric space group of *Pna*2₁ (No. 33) and *P62m* (No. 189), respectively (Table 1 and Supplementary Table 1). Interestingly, the molecular formula of both phases was determined as $\text{Ba}_3\text{Mg}_3(\text{BO}_3)_3\text{F}_3$ through structure solutions, which have the same simplest molecular formula with BaMgBO_3F (monoclinic, *Cc*) reported by Li. et al.³⁴. And the relatively low temperature factors and residual factors verify the correctness of those two crystal models, which also indicates the existence of two polymorphs. Furthermore, the BMBF polymorphs and phase transitions are further confirmed by high-temperature in situ powder X-ray diffraction and thermal expansion coefficients experiment: based on the results of thermal gravimetric and differential scanning calorimetry analysis (Fig. 1a), we make circular heating and cooling the *Pna*2₁-BMBF samples in the region of 100–650 °C. When the temperature rises to 500 °C, the *Pna*2₁-BMBF phase start to transfer into *P62m*-BMBF phase, and *P62m*-BMBF is stable up to 650 °C. When the temperature begins to decrease, *P62m*-BMBF phase can also transfer into *Pna*2₁-BMBF, indicating the reversibility of this phase transition behavior. More intuitively, the disappearance and appearance of X-ray diffraction peaks at about $2\theta = 23.690, 26.994, \text{ and } 27.686^\circ$ in BMBF series can help us to judge this phase transition (Fig. 1b, c). The measured average thermal expansion coefficients based on the three as-polished (100), (010), and (001) wafers occur sudden change at about 450 °C, which is caused by the phase transitions of BMBF series (Fig. 1d).

Crystal structures of *Pna*2₁- and *P62m*-BMBF. The structural evolution among SBBO, *Pna*2₁-, and *P62m*-BMBF are shown in Fig. 2, which verifies the validity of structure-oriented design strategy. As shown in Fig. 2a, b, e, BMBF series possess a similar

Table 1 Crystallographic data for *Pna*2₁- and *P62m*- $\text{Ba}_3\text{Mg}_3(\text{BO}_3)_3\text{F}_3$

Empirical formula	$\text{Ba}_3\text{Mg}_3(\text{BO}_3)_3\text{F}_3$	$\text{Ba}_3\text{Mg}_3(\text{BO}_3)_3\text{F}_3$
Formula weight	718.38	718.38
Crystal system	Orthorhombic	Hexagonal
Space group	<i>Pna</i> 2 ₁ (No. 33)	<i>P62m</i> (No. 189)
<i>a</i> (Å)	8.0740(3)	8.804(3)
<i>b</i> (Å)	15.3072(7)	8.804(3)
<i>c</i> (Å)	8.8218(4)	4.025(3)
<i>Z</i>	4	1
Volume (Å ³)	1090.29(8)	270.2(2)
Reflns collected/unique	11,605/2377	1695/261
Completeness (%)	99.8	100
Goodness of fit on F^2	1.233	1.251
Final <i>R</i> indices	$R_1 = 0.0118,$	$R_1 = 0.0204,$
$[F_o^2 > 2\sigma(F_o^2)]^a$	$wR_2 = 0.0249$	$wR_2 = 0.0394$
<i>R</i> indices (all data) ^a	$R_1 = 0.0120,$	$R_1 = 0.0207,$
	$wR_2 = 0.0250$	$wR_2 = 0.0395$

^a*R* means residual factor

^a $R_1 = \sum ||F_o| - |F_c|| / \sum |F_o|$ and $wR_2 = [\sum w(F_o^2 - F_c^2)^2 / \sum wF_o^4]^{1/2}$ for $F_o^2 > 2\sigma(F_o^2)$

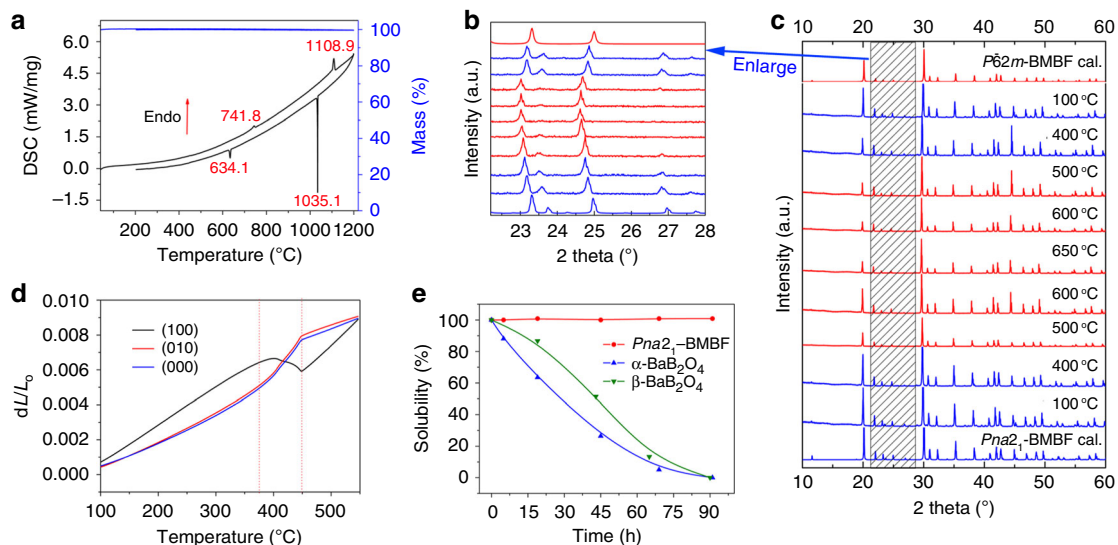


Fig. 1 Basic physicochemical properties of $\text{Ba}_3\text{Mg}_3(\text{BO}_3)_3\text{F}_3$. **a** Thermal gravimetric and differential scanning calorimetry (DSC) curves. Endo means the endothermic direction. There are two remarkable endothermic peaks (741.8 and 1108.9 °C) on the heating curve and two exothermic peaks (634.1 and 1035.1 °C) on the cooling curve, respectively. **b, c** High-temperature in situ powder X-ray diffraction data circularly collected in the region of 100–650 °C. The experimental and calculated powder X-ray diffraction patterns of $Pna2_1\text{-Ba}_3\text{Mg}_3(\text{BO}_3)_3\text{F}_3$ (blue lines) and $P\bar{6}2m\text{-Ba}_3\text{Mg}_3(\text{BO}_3)_3\text{F}_3$ (red lines). The enlarged version of **c** in the 2θ region from 22.3 to 28.2° is shown in **b** to better understand the phase transition behavior between two polymorphs. **d** Thermal expansion measurements tested by (100), (010), and (001) $Pna2_1\text{-Ba}_3\text{Mg}_3(\text{BO}_3)_3\text{F}_3$ crystal plates. dL and L_0 mean the change in crystal plates length and initial length of crystal plates, respectively. **e** Solubility experiments of $Pna2_1\text{-Ba}_3\text{Mg}_3(\text{BO}_3)_3\text{F}_3$, $\alpha\text{-BaB}_2\text{O}_4$ and $\beta\text{-BaB}_2\text{O}_4$

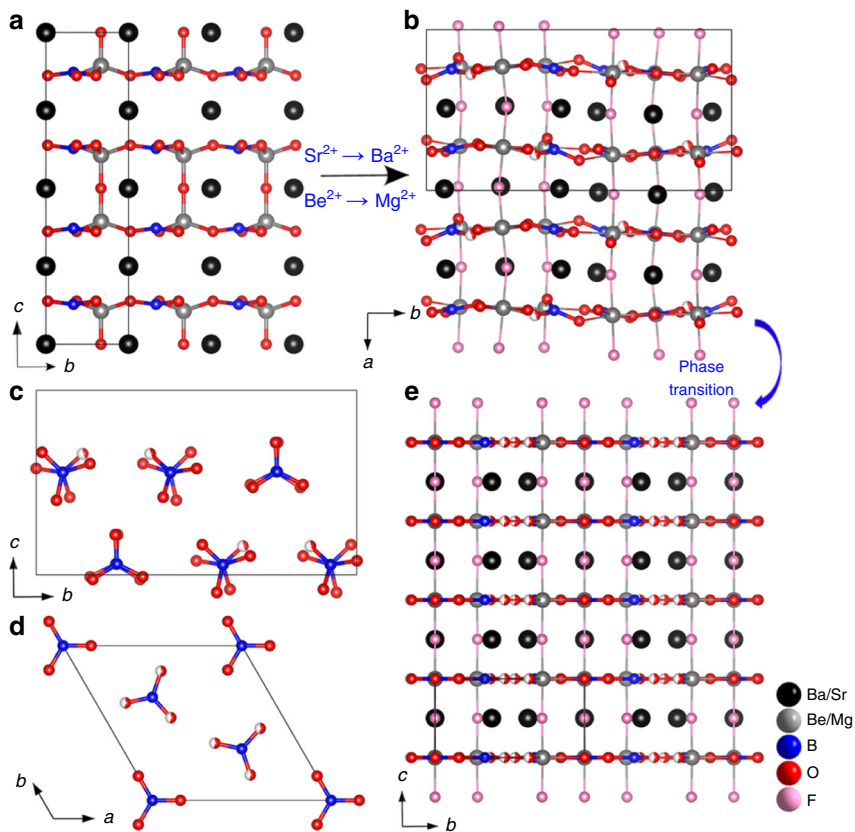


Fig. 2 Crystal structural features of $Pna2_1\text{-Ba}_3\text{Mg}_3(\text{BO}_3)_3\text{F}_3$. **a, b** The structural evolution from $\text{Sr}_2\text{Be}_2\text{B}_2\text{O}_7$ to $Pna2_1\text{-Ba}_3\text{Mg}_3(\text{BO}_3)_3\text{F}_3$. **c, d** The orientation of $[\text{BO}_3]^{3-}$ groups in $Pna2_1\text{-}$ and $P\bar{6}2m\text{-Ba}_3\text{Mg}_3(\text{BO}_3)_3\text{F}_3$, respectively. **e** The layered structure of derivative $P\bar{6}2m\text{-Ba}_3\text{Mg}_3(\text{BO}_3)_3\text{F}_3$ derived by phase transition from $Pna2_1\text{-Ba}_3\text{Mg}_3(\text{BO}_3)_3\text{F}_3$

layered crystal structures, their crystal structures are both composed of ${}^2_{\infty}[\text{Mg}_3\text{O}_2\text{F}_3(\text{BO}_3)_2]$ layers (Supplementary Figure 1) along the *a*-axis for *Pna*2₁-BMBF and *c*-axis for *P6*2*m*-BMBF, and those single layers are further connected by the Mg–F bonds to construct a three-dimensional framework with tunnels running along the *c* (or *a*)-axis. In the asymmetric unit of *Pna*2₁-BMBF, the Ba, Mg, B, and F atoms occupy three crystallographically unique positions, for the O atoms there are nine unique positions. While for *P6*2*m*-BMBF with higher symmetry, the Ba, Mg, B, O, and F atoms occupy one, one, two, two, and one unique positions (Supplementary Tables 2, 3, 5, and 6). In both BMBF polymorphs, the B atoms possess only one coordination type, the $[\text{BO}_3]^{3-}$ triangles (Fig. 2c, d). The B–O bond distances and O–B–O bond angles locate in the range from 1.341 to 1.395 Å, 117.6 to 120.9 ° for *Pna*2₁-BMBF, and 1.349 to 1.381 Å, 117.0 to 122.8 ° for *P6*2*m*-BMBF, respectively (Supplementary Tables 4 and 7). The Mg atoms in both polymorphs are six-coordinated into the MgO_4F_2 octahedra with four O and two F atoms locating in the equatorial and axial positions, respectively. Three MgO_4F_2 units share three O atoms to generate a six-membered ring cluster $\text{Mg}_3\text{O}_9\text{F}_6$ (Supplementary Figure 2), then those clusters link together via the axial Mg–F bonds to build an isolated ${}^3_{\infty}[\text{Mg}_3\text{O}_9\text{F}_3]$ triangular prism (Supplementary Figure 3). Interestingly, two $[\text{BO}_3]^{3-}$ units locate in and out of the six-membered ring $\text{Mg}_3\text{O}_9\text{F}_6$ to form polymer and further polymerize into ${}^2_{\infty}[\text{Mg}_3\text{O}_2\text{F}_3(\text{BO}_3)_2]$ infinite layers, and the connection is by bridging Mg–F bonds to form a three-dimensional multi-layered structure. All the Ba atoms are coordinated into BaO_nF_m (*m* + *n* = 10 and 11) polyhedra, located between the adjacent ${}^2_{\infty}[\text{Mg}_3\text{O}_2\text{F}_3(\text{BO}_3)_2]$ layers, which is quite like the arrangement of the Sr atoms in SBBO¹.

Structurally, the triangular $[\text{BO}_3]^{3-}$ units in both *Pna*2₁- and *P6*2*m*-BMBF adopt nearly coplanar configuration. This is propitious to generate large SHG response and birefringence

because of the strong anisotropy resulting from their different polarizabilities in different directions, which is similar to the NLO materials containing π -planar triangular $[\text{CO}_3]^{2-}$ ^{35,36}. The F–Mg–F bonds act as bridge-linking role to connect the neighboring layers, which is similar to the $[\text{B}_2\text{O}_5]^{4-}$ dimers in $\text{LiNa}_5\text{Be}_{12}\text{B}_{12}\text{O}_{33}$ ³⁷ and the $[\text{B}_3\text{O}_6]^{3-}$ groups in $\text{Cs}_3\text{Zn}_6\text{B}_9\text{O}_{21}$ ^{38,39}. Further, the electrostatics force of the interaction between layers in *Pna*2₁- and *P6*2*m*-BMBF was evaluated and $|F_{\text{Mg-F}}|$ is stronger than that of $|F_{\text{K-F}}|$ in KBBF (Supplementary Table 8), indicating that the electrostatic interactions between Mg–F bonds in *Pna*2₁- and *P6*2*m*-BMBF provide better linkage of neighboring layers, which is favorable to improve the layering tendency and the same results can be concluded from the ease of the growth of block-like crystals of BMBF series than that of KBBF.

Crystal growth and optical quality of *Pna*2₁-BMBF. After various attempts, *Pna*2₁-BMBF crystal with dimensions up to $16 \times 14 \times 8 \text{ mm}^3$ has been grown at the optimal conditions (Fig. 3a). *Pna*2₁-BMBF crystal has never cracked during cutting and polishing into (100), (010), and (001) wafers (Fig. 3b). The crystallization quality of the as-grown crystal was checked by the X-ray rocking curve. As shown in Fig. 3c, the full-width at half-maximum on (100) face of *Pna*2₁-BMBF crystal was measured to be 18", indicating high crystalline quality. The conoscopic interference pattern (Fig. 3d) shows that the as-grown *Pna*2₁-BMBF crystal is biaxial, optical homogeneous, and does not have any strain inside. When taken together, *Pna*2₁-BMBF crystal shows high optical quality, and the optical measurements based on this crystal are reliable.

High performances as UV NLO materials. *Pna*2₁-BMBF was subjected to physicochemical property characterizations based on the single-crystal level.

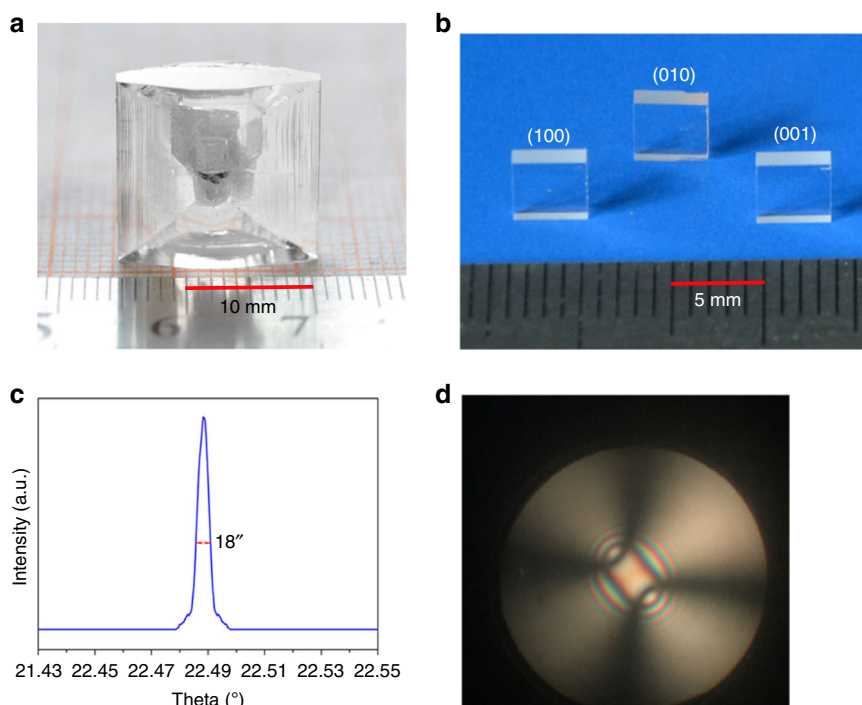


Fig. 3 The as-grown single crystal and optical quality experiments of *Pna*2₁-Ba₃Mg₃(BO₃)₃F₃. **a** Photograph of the as-grown crystal with dimensions up to $16 \times 14 \times 8 \text{ mm}^3$ grown by the top-seeded solution growth method. **b** The cut and polished (100), (010), and (001) wafers with dimensions up to $4 \times 4 \times 1 \text{ mm}^3$. The crystals were cut plane parallel and polished to optical quality using a Unipol-300 grinding/polishing machine. **c** The high-resolution X-ray diffraction rocking curve for (100) wafer. The full-width at half-maximum on (100) face of the *Pna*2₁-Ba₃Mg₃(BO₃)₃F₃ crystal is about 18", indicating high crystalline quality. **d** The conoscopic interference pattern of *Pna*2₁-Ba₃Mg₃(BO₃)₃F₃ crystal. All the images and elements of them were created by ourselves

Thermal expansion coefficients are vital parameters for crystal growth and application in devices. As can be seen in Fig. 1d, the average thermal expansion coefficients in the region from 100 to 450 °C are evaluated to be $\alpha_a = \alpha(100) = 2.17 \times 10^{-5} \text{ K}^{-1}$, $\alpha_b = \alpha(010) = 1.63 \times 10^{-5} \text{ K}^{-1}$, and $\alpha_c = \alpha(001) = 1.53 \times 10^{-5} \text{ K}^{-1}$, respectively. The value of α_a/α_c is about 1.43 for *Pna2*₁-BMBF crystal, which is smaller than that of β -BaB₂O₄ (β -BBO) ($\alpha_c/\alpha_a = 9$)⁴⁰. Therefore, *Pna2*₁-BMBF crystal exhibits a more favorable anisotropic thermal expansion, which will effectively protect the crystals from cracking caused by thermal expansion during crystal growth and optical devices fabrication.

To study the water solubility of *Pna2*₁-BMBF, we dipped the target *Pna2*₁-BMBF (0.113 g) crystal as well as the references α - and β -BBO crystals (0.159 and 0.105 g) into 20 mL de-ionized water at room temperature. As plotted in Fig. 1e, the weight of *Pna2*₁-BMBF did not change in the measured time ranges, while for α - and β -BBO crystals, they were dissolved in water in 90 h. These indicate that *Pna2*₁-BMBF is chemically stable and not soluble in the water.

We carried out the SHG measurements by the Kurtz–Perry method⁴¹ with incident lasers at $\lambda = 1064 \text{ nm}$. Meanwhile, the well-known NLO material KH₂PO₄ (KDP) was used as the reference. The comparison of SHG signals produced by *Pna2*₁- and *P62m*-BMBF polycrystalline samples in the same particle sizes ranging from 200 to 250 μm reveals that *Pna2*₁- and *P62m*-BMBF exhibit suitable SHG responses of ~ 1.8 and $2.0 \times \text{KDP}$, respectively. Such SHG responses are large enough for the

applications of UV NLO materials and it is also comparable to those reported borates with deep-UV cutoff edges, such as KBBF ($1.26 \times \text{KDP}$)¹⁹, LiNa₅Be₁₂B₁₂O₃₃³⁷ ($1.4 \times \text{KDP}$), and Li₄Sr(BO₃)₂ ($2 \times \text{KDP}$)²². According to the results, the SHG efficiency increases with the raising particle sizes, indicating that both BMBF polymorphs exhibit type I phase-matching behavior in 1064 nm incident lasers. In addition, the effective NLO coefficients (d_{eff}) of *Pna2*₁- and *P62m*-BMBF crystal are estimated to be about 1.3 and $1.4 \times \text{KDP}$ according to the square roots of the ratios of their corresponding SHG signal intensities. In order to verify the results, large sizes of single crystals should be grown and cut to evaluate the SHG coefficients based on the crystal level, which is discussed in detail in the following parts.

The as-grown crystals were cut and optically polished to 1 mm thickness for the spectrum measurement. As presented in Fig. 4b, the *Pna2*₁-BMBF crystal exhibits a broad transmission of 184–3780 nm, indicating that the application of *Pna2*₁-BMBF crystal can cover a spectral range from UV to near-infrared. Obviously, the UV cutoff edge of *Pna2*₁-BMBF is about 184 nm, which is 5 nm shorter than that of β -BBO (189 nm) in the same measured condition. And also the high transmittance of *Pna2*₁-BMBF in the UV spectral range makes it possible to be applied as a UV NLO material. The short cutoff edge is beneficial to obtain high LDT, therefore, LDT measurements were carried out using a pulsed nanosecond laser (1064 nm, 10 ns, and 10 Hz). A well-polished high-quality (001) wafer of *Pna2*₁-BMBF has a LDT of

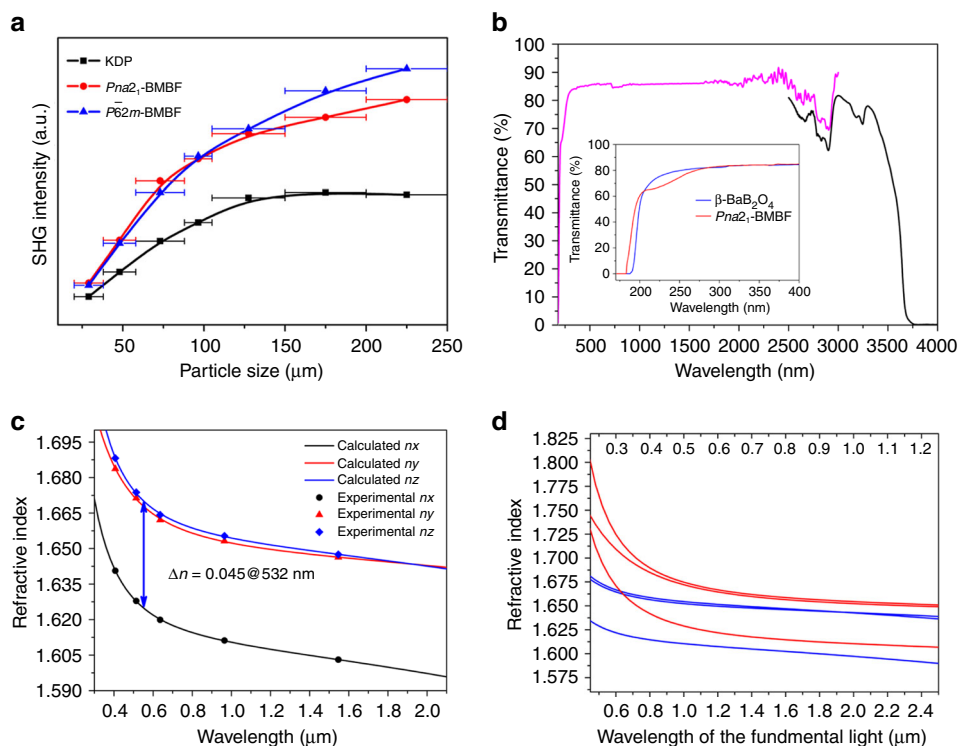


Fig. 4 Optical properties of *Pna2*₁-Ba₃Mg₃(BO₃)₃F₃. **a** Powder second-harmonic generation data for Ba₃Mg₃(BO₃)₃F₃ polymorphs at 1064 nm laser radiation. The well-known NLO material KH₂PO₄ (KDP) was used as the reference. The curves are drawn to guide the eyes, and are not fit to the data. The error bars from left to right correspond to sieved crystal particle size ranges: 20–38; 38–55; 55–88; 88–105; 105–150; 150–200; and 200–250 μm . **b** Transmission spectrum of *Pna2*₁-Ba₃Mg₃(BO₃)₃F₃ crystal. Transmittance curve (magenta line) between 180 and 2500 nm was collected by a Shimadzu Solid Spec-3700DUV Spectrophotometer. Transmittance curve (black line) between 2500 and 4000 nm was collected by a Shimadzu IRAffinity-1 spectrometer. Inset gives transmittance curves between 170 and 400 nm for *Pna2*₁-Ba₃Mg₃(BO₃)₃F₃ (red line) and β -BaB₂O₄ (blue line). The ultraviolet cutoff edge of *Pna2*₁-Ba₃Mg₃(BO₃)₃F₃ is about 184 nm, which is 5 nm shorter than that of β -BBO (189 nm). **c** The refractive index dispersion curves for the *Pna2*₁-Ba₃Mg₃(BO₃)₃F₃ crystal. **d** The refractive index dispersion curves for fundamental (blue lines) and the second-harmonic (red lines) light. Based on the Sellmeier equations, when considering the type I phase-matching condition, $n(\omega) = n(2\omega)$, the shortest type I phase-matching wavelengths in the *xz* and *xy* plane are evaluated to be 310 and 322 nm

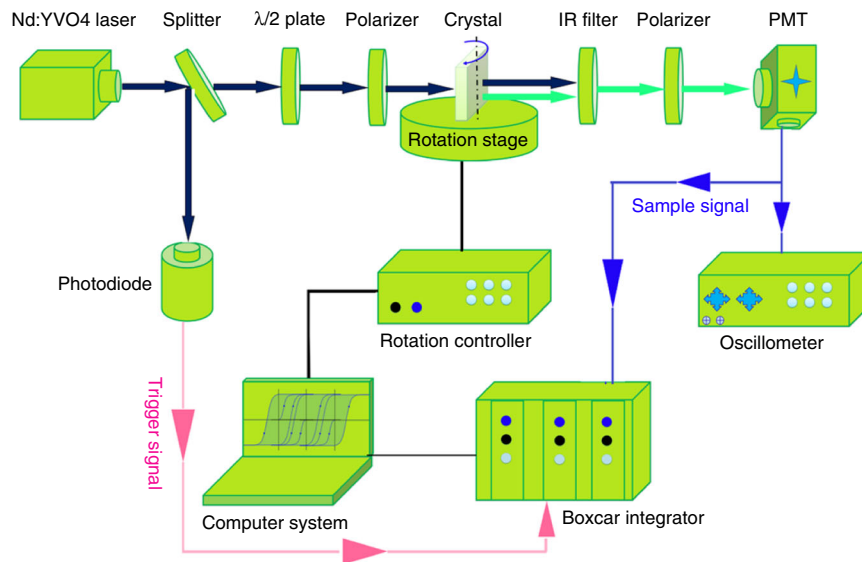


Fig. 5 Schematic diagram of the Maker fringe experiment using an Nd:YVO₄ laser. A Q-switched Nd:YVO₄ laser system was adopted as fundamental light source with the following experimental conditions: fundamental wavelength: 1064 nm; repetition frequency: 10 kHz; and pulse width: 10 ns. The second-harmonic signal, which changed with rotation angle of *Pna*2₁-Ba₃Mg₃(BO₃)₃F₃ crystal, was detected by a photomultiplier tube, averaged by a fast-gated integrator and boxcar integrator, and then recorded by computer system. The *Pna*2₁-Ba₃Mg₃(BO₃)₃F₃ crystal is at the waist of the fundamental light with a beam diameter of 1.0 mm

~6.2 GW/cm², which is comparable to β-BBO crystal (~6.0 GW/cm²) at the same experimental conditions.

The refractive indices of *Pna*2₁-BMBF were measured using prism coupling method. As it follows the inequality $n_z - n_y < n_y - n_x$, which depicts that *Pna*2₁-BMBF is a negative biaxial crystal (consistent with results of conoscopic interference patterns), with the birefringence ($\Delta n = n_z - n_x$) ranging from 0.044@1064 nm to 0.045@532 nm and the values are comparable with those of the commercial UV NLO materials LiB₃O₅ and CsLiB₆O₁₀ ($\Delta n = 0.045$ and 0.049@1064 nm)¹⁰. A least-square method was used to fit the dispersion parameters of the refractive indices, n_i , using the Sellmeier Eq. (1):

$$n_i^2 = A + \frac{B}{\lambda^2 - C} - D\lambda^2 \quad (1)$$

where λ represents the wavelength in units of μm , and A , B , C , and D are the Sellmeier parameters. The Sellmeier Eq. (1) deduced by the least-square fitting of all the measured refractive indices have been fitted as:

$$\begin{aligned} n_x^2 &= 2.58654 + \frac{0.01672}{\lambda^2 - 0.00904} - 0.00987\lambda^2 \\ n_y^2 &= 2.71284 + \frac{0.02264}{\lambda^2 + 0.01829} - 0.00486\lambda^2 \\ n_z^2 &= 2.72604 + \frac{0.01908}{\lambda^2 - 0.01344} - 0.00819\lambda^2 \end{aligned} \quad (2)$$

The calculated and experimental values of the refractive indices at five different wavelengths are summarized in Supplementary Table 9. The calculated values are consistent with experimental ones to the fourth decimal place, which indicates that the fitted Sellmeier equations based on the current data are reliable (Fig. 4c). Based on above fitted Sellmeier equations, when considering the type I phase-matching condition, $n(\omega) = n(2\omega)$, the shortest type I phase-matching wavelengths in the xz and xy plane are evaluated to be 310 and 322 nm (Fig. 4d), respectively.

Therefore, the *Pna*2₁-BMBF crystal can generate 532 and 355 nm light by direct second and third harmonic generation from a 1064 nm laser.

In order to determine the individual NLO coefficients of *Pna*2₁-BMBF, Maker fringe measurements were carried out. The schematic of the Maker fringe measurement system is shown in Fig. 5. For the SHG coefficient measurements, the orientation of the crystals and the relationships of P_ω and $P_{2\omega}$ are shown in Fig. 6a, c. The (001)-cut and (100)-cut plane-parallel uncoated plates of *Pna*2₁-BMBF crystals (4 mm × 4 mm × 1 mm) were used to measure the related NLO coefficients. And also a (110)-cut plate (5 mm × 5 mm × 2 mm) of the KDP crystal was used to measure the d_{36} (KDP) NLO coefficient as the reference. By fitting the calculated Maker fringes based on the current measurements and calculations, the NLO coefficient of the *Pna*2₁-BMBF crystal relative to d_{36} (KDP) has been determined as $d_{33} = 1.3 \times d_{36}$ (KDP) (Fig. 6b, d). However, the Maker fringe for d_{31} is too weak to be observed. As d_{36} coefficient of KDP is 0.39 pm/V, the absolute NLO coefficients of *Pna*2₁-BMBF crystal based on the measurements and calculations are evaluated to be $d_{33} = 0.51$ pm/V.

Discussion

In order to achieve a deep investigation about the structure-property relationship, theoretical calculations based on density functional theory methods were performed^{42–44}. The total and partial density of states projected on the constitutional atoms of *Pna*2₁-BMBF crystal are given in Fig. 7a. Clearly, the energy bands can be divided into several regions. The uppermost part of valence bands from -7.5 to 0 eV is essentially dominated by O 2p states and an appreciable contribution of F 2p orbitals with a small amount of B 2p states. The obvious narrow band with sharp peak locates at about -10.7 eV entirely dominated by Ba 5p orbitals and also with a small contribution of O 2p states. The last part from -19.4 to -15.9 eV is mainly generated from O 2s, O 2p, and B 2s, B 2p, indicating strong sp hybridization of the B and O orbitals in the [BO₃]³⁻ groups. While the bottom of the conduction band is essentially composed of Ba 5d, Ba 5s, B 2p, and O 2p orbitals. In principle, the optical properties are mainly

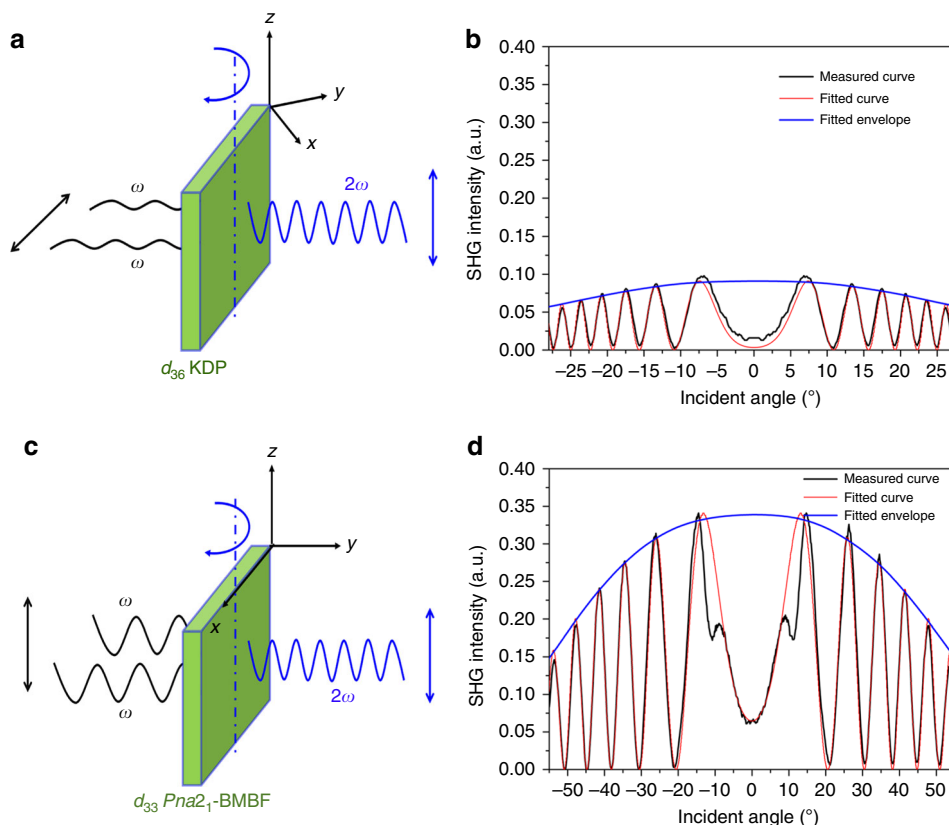


Fig. 6 Maker fringe measurement for $Pna2_1$ - $Ba_3Mg_3(BO_3)_3F_3$ crystal. **a, c** The orientations of as-grown crystal plates for measuring the NLO coefficients. **b, d** The measured and calculated Maker fringe data as well as fitted envelope for d_{36} of KH_2PO_4 (KDP) and d_{33} of $Pna2_1$ - $Ba_3Mg_3(BO_3)_3F_3$. The data were fitted according to the Maker fringe theory and the detailed fitting procedure is available in the Methods section

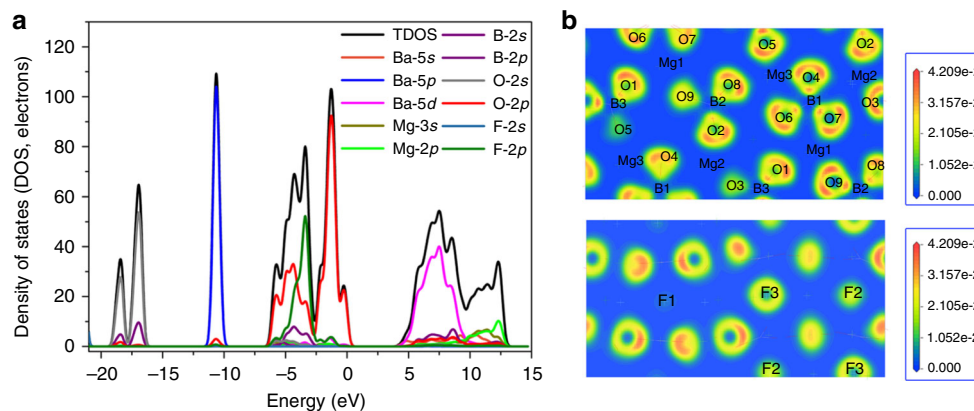


Fig. 7 Theoretical calculation results of $Pna2_1$ - $Ba_3Mg_3(BO_3)_3F_3$. **a** Partial and total density of states with the energy region from -22 to 15 eV. **b** The electron localization function diagrams slice along the bc plane (top of **b**) with the slice position of $(5.70841, 7.67893, 4.35171)$ and ab plane (bottom of **b**) with the slice position of $(4.02830, 7.63500, 7.43644)$, respectively. Isovalue increases from blue to red, and the maximum electron localization function value is scaled to 4.209×10^{-2} for the two electron localization function diagrams

determined by the electronic transitions among the states near Fermi level, which are mainly occupied by the O 2p nonbonding orbitals, B–O hybridization states and Ba 5d states in $Pna2_1$ -BMBF. Besides, the interatomic interactions within the BO_3 units and MgO_4F_2 octahedra can be clearly visualized by the electron localization function diagrams. Results show the ionic character of Mg–O and Mg–F bonds in the MgO_4F_2 octahedra as well as the covalent nature of B–O bonds in the $[BO_3]^{3-}$ units (Fig. 7b). Through the Mulliken population analysis, the same conclusions

can also be substantiated by the calculated overlap populations for Mg–F, Mg–O and B–O, which are 0.12–0.21, 0.21–0.55, and 0.85–0.97, respectively (higher populations reflect stronger covalence).

The NLO properties of $Pna2_1$ -BMBF were also calculated using a theoretical technique under the static limit within the length gauge. The calculated SHG tensors are evaluated to be $d_{33} = 0.47$, $d_{32} = -0.39$, and $d_{31} = 0.09$ pm/V, respectively. These values are well consistent with experimental values presented above ($d_{33} =$

0.51 pm/V). The SHG density analysis can be used to intuitively and accurately display the SHG-contributed orbitals for an NLO crystal. Furthermore, we investigated the SHG origin of $Pna2_1$ -BMBF from the perspective of orbital analysis using SHG density analysis. And the SHG process is denoted by two virtual transition processes, namely virtual electron (VE) and virtual hole processes. The contributions of VE process to d_{31} , d_{32} , and d_{33} SHG tensors are up to 83.7%, 81.6%, and 86.5%, respectively, indicating that the SHG effects of three tensors mainly originate from the VE processes. Thus, only the largest d_{33} SHG tensor of VE process is analyzed and the results are drawn in Fig. 8. In the occupied states, the nonbonding $2p$ orbitals of O (1, 2, 3, 5, 8, 9) atoms in $[B(2)O_3]^{3-}$ and $[B(3)O_3]^{3-}$ groups give more dominant contributions to the SHG effects, while for the occupied states, π orbitals of the $[B(1, 2, 3)O_3]^{3-}$ units as well as $2p$ orbitals of F (1, 2, 3) atoms in the MgO_4F_2 octahedra give more dominant contributions for the SHG effects, revealing the p –(p , π^*) charge-transfer excitation mechanism in $Pna2_1$ -BMBF. Both occupied and unoccupied states of the Ba cations, in analogy to alkali metal and alkali earth metal ions in other NLO crystals, have very little contribution on the SHG effect, which agrees well with the anionic group theory¹⁰. To sum up, the large SHG response of $Pna2_1$ -BMBF can be regarded as the synergistic effects of the planar $[BO_3]^{3-}$ and distorted MgO_4F_2 octahedra.

In summary, by starting from the SBBO structure, we designed and synthesized two beryllium-free SBBO-like borates through chemical cosubstitution strategy. A high-quality $Pna2_1$ -BMBF crystal with dimensions up to $16 \times 14 \times 8$ mm³ has been grown by the top-seeded solution growth method with a BaF_2 - H_3BO_3 -LiF flux system. Linear and nonlinear optical measurements reveal a sufficiently large SHG coefficient ($d_{33} = 0.51$ pm/V), suitable birefringence (0.045@532 nm), type I phase-matchability, and

chemical stability. Remarkably, $Pna2_1$ -BMBF has a large LDT (~ 6.2 GW/cm²), a deep-UV cutoff edge ($\lambda \sim 184$ nm), a weak anisotropic thermal expansion as well as the capacity of insolubility in water, these optical properties could be comparable or superior to that of commercial NLO materials β -BBO (Supplementary Table 10). Thus, these merits on optical properties make $Pna2_1$ -BMBF a promising UV NLO material.

Methods

Synthesis and crystal growth. Polycrystalline samples of targeted $Pna2_1$ -BMBF were synthesized through solid-state reaction method by mixing the raw materials BaF_2 , $BaCO_3$, MgO , and H_3BO_3 according to the molar ratio of 3:3:6:6. The mixture was preheated at 400 °C for 48 h. After that, the temperature was gradually raised to 600 °C for $Pna2_1$ -BMBF, with several intermediate mixings and grindings. Single crystals of $Pna2_1$ -BMBF were grown by top-seeded solution growth method with the flux BaF_2 - H_3BO_3 -LiF at a molar ratio of $Pna2_1$ -BMBF/ H_3BO_3 / BaF_2 /LiF = 1:1:0.5:3. A mixture of $Pna2_1$ -BMBF polycrystalline samples, BaF_2 , H_3BO_3 , and LiF were placed into a $\Phi 30 \times 30$ mm platinum crucible and melted at 750 °C in a temperature-programmable electric furnace. The solution was held at 750 °C for 24 h to form a homogeneous solution. After that, cooled to 715 °C and dipped the $Pna2_1$ -BMBF seed crystal into the solution and held for 2 h that allowed the seed crystal surface to melt. The solution was slowly cooled to the saturation temperature about 712 °C. Then the $Pna2_1$ -BMBF crystal was grown by cooling the solution at a rate of 0.2 °C/d to 706 °C. When the growth procedure finished, the $Pna2_1$ -BMBF crystal was drawn out of the solution and cooled down to room temperature at a rate of 20 °C/h. While for $P62m$ -BMBF single crystals, the loaded compositions are $Ba(NO_3)_2$ (0.5227 g, 2 mmol), BaF_2 (0.3507 g, 2 mmol), MgO (0.0403 g, 1 mmol) and H_3BO_3 (0.4328 g, 7 mmol). All the reagents were mixed homogeneously and transferred to a platinum crucible. The samples were heated to 880 °C in 24 h and held at this temperature for 72 h and then cooled to 700 °C at a rate of 1.0 °C/h, after that, cooled to room temperature at a rate of 15 °C/h. During the process of crystallization, colorless and transparent $P62m$ -BMBF crystals were formed in the platinum crucible.

Characterization. The selected single crystals with dimensions up to $0.12 \times 0.10 \times 0.01$ mm³ for $Pna2_1$ -BMBF and $0.16 \times 0.07 \times 0.06$ mm³ for $P62m$ -BMBF were glued on glass fibers for structure determination by single-crystal X-ray diffractometer. An APEX II CCD diffractometer equipped with monochromatic Mo K α radiation was used for the single-crystal data collection. The Bruker Suite software package was used to reduce the collected data. The numerical absorption corrections were carried out with the SADABS program and integrated with the SAINT program⁴⁵. The original structures were established by the direct method and refined by the full-matrix least-squares program on SHELXL⁴⁶. The PLATON program was used for checking the possible missing symmetry elements, but no higher symmetries were found⁴⁷. Investigation of the thermal behavior $Pna2_1$ -BMBF crystal was performed using a NETZSCH STA 449 C simultaneous thermal analyzer. The sample of 6.5 mg was enclosed in a platinum crucible and heated from 40 to 1200 °C at a rate of 5 °C/min. The measurements were carried out in an atmosphere of flowing N₂. The powder X-ray diffraction data of $Pna2_1$ -BMBF were collected at room temperature using an automated Bruker D2 X-ray diffractometer (Supplementary Figure 4). The transmittance spectra of $Pna2_1$ -BMBF water were collected by a Solid Spec-3700DUV spectrophotometer for the range of 180–2500 nm in an atmosphere of flowing N₂ and by a Shimadzu IRAffinity-1 Fourier spectrometer for the range extended from 2500 to 4000 nm (Supplementary Figure 5). The powder SHG measurements for targeted $Pna2_1$ - and $P62m$ -BMBF were carried out on the basis of the Kurtz–Perry method⁴¹. Polycrystalline samples of $Pna2_1$ - and $P62m$ -BMBF were ground and sieved into the following particle size ranges: 20–38; 38–55; 55–88; 88–105; 105–150; 150–200; and 200–250 μ m. During the measurement, $Pna2_1$ - and $P62m$ -BMBF samples were irradiated with a Q-switched Nd:YAG laser with light wavelength of 1064 nm. Then the intensity of the frequency-doubled of 532 nm output emitted from $Pna2_1$ - and $P62m$ -BMBF were recorded by a digital oscilloscope equipped with a photomultiplier tube. The microcrystalline KDP samples with the same particle sizes were used as references. For LDT test, the crystals were cut plane parallel and polished to optical quality using a Unipol-300 grinding/polishing machine. A Q-switched Nd:YAG laser with a pulse width of 10 ns and repetition frequency of 10 kHz was employed as the fundamental light source (1064 nm). The second-harmonic signal generated from the sample wafer was detected by a side window photomultiplier tube, averaged by a fast-gated integrator and boxcar average, and then automatically recorded by a computer. A cut-KDP (110) wafer was used as a reference. The refractive index measurements of $Pna2_1$ -BMBF were carried out using (100), (010), and (001) crystal plates on the Metricon model 2010/M prism coupler (Metricon Co.) at five wavelengths (406.9, 514.0, 636, 964.8, and 1546.7 nm), and the accuracy of the measurements is estimated to be 2×10^{-4} . Maker fringe measurements of $Pna2_1$ -BMBF were performed on two crystal wafers cut perpendicular to the *a*- and *b*-crystallographic axes in order to measure d_{31} , d_{32} , and d_{33} NLO coefficients. Then, the data were fitted according to the Maker fringe theory. The detected second-

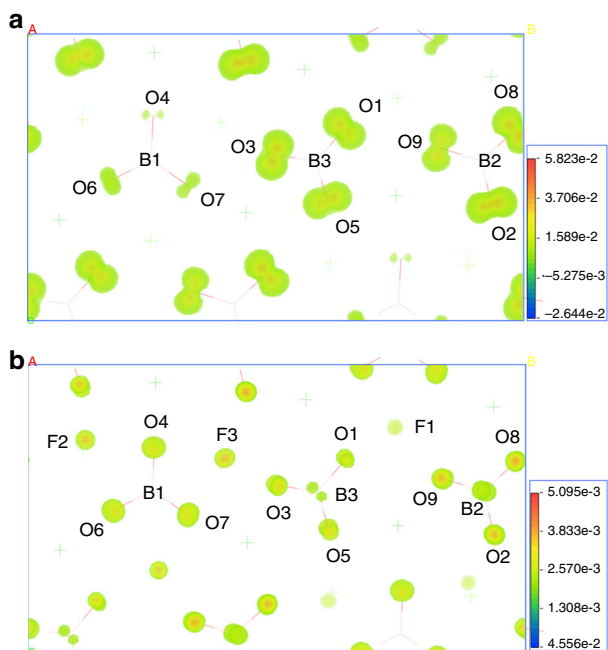


Fig. 8 The second-harmonic generation density analysis of $Pna2_1$ - $Ba_3Mg_3(BO_3)_3F_3$. **a** The density maps of the occupied orbitals in virtual electron process of the second-harmonic generation tensor d_{33} . **b** The density maps of the unoccupied orbitals in virtual electron process of the second-harmonic generation tensor d_{33} of $Pna2_1$ - $Ba_3Mg_3(BO_3)_3F_3$. Isovalue increases from blue to red, and the maximum electron localization function values are scaled to 5.823×10^{-2} for occupied orbitals (**a**) and 5.095×10^{-2} for unoccupied orbitals (**b**), respectively

harmonic power $P_{2\omega}$ is expressed as the following Eq.(3):

$$P_{2\omega}(\theta) = \frac{512\pi^2}{c^2 w^2} d^2 P_{\omega}^2 f(n, \theta) \sin^2 \Psi \quad (3)$$

$$f(n, \theta) = \frac{1}{(n_{\omega}^2 - n_{2\omega}^2)^2} t_{\omega}^4 T_{2\omega} p^2(\theta) R(\theta) \beta(\theta) \quad (4)$$

where c is the speed of light in vacuum, w is the radius of light beam, n_{ω} and $n_{2\omega}$ are the refractive indices under the fundamental and harmonic wavelength, d is the NLO coefficient, P_{ω} is the fundamental beam power, $\Psi = 2\pi L(n_{\omega} \cos \theta_{\omega} - n_{2\omega} \cos \theta_{2\omega})/\lambda_{\omega}$, and $\sin^2 \Psi$ determines the minima oscillating position. t_{ω} and $t_{2\omega}$ are the transmission coefficients of fundamental wave and harmonic wave, $p(\theta)$ is the projection factor, $R(\theta)$ is the incident multiple-reflection correction, and $\beta(\theta)$ is the beam size correction. The $f(n, \theta)$ part depicts the envelope of the Maker fringe. By fitting the calculated and measured Maker fringes, a constant, $C = 512\pi d^2 P_{\omega}^2 / (c w^2)$ can be obtained. The magnitude of NLO coefficients of $Pna2_1$ - $Ba_3Mg_3(BO_3)_3F_3$ can be determined relatively to d_{36} of KDP crystal, and the coefficient equation can be expressed as:

$$d_{\text{sample}} = \sqrt{\frac{C_{\text{sample}}}{C_{\text{KDP}}}} d_{36}(\text{KDP}) \quad (5)$$

Computational methods. First-principles calculations of $Pna2_1$ -BMBF based on density functional theory were performed by a planewave pseudopotential calculation package CASTEP⁴⁸. The exchange and correlation effects were treated by Perdew–Burke–Ernzerhof in the generalized gradient approximation⁴⁹. The interactions between the ionic cores and electrons were described by norm-conserving pseudopotentials⁵⁰. The cutoff energy for the planewave basis was 990 eV and the Brillouin zone was sampled by $4 \times 2 \times 3$ Monkhorst-Pack k -point.

Data availability. The authors declare that the data supporting the findings of this study are available within the article and Supplementary Information files, or from the corresponding authors upon reasonable request.

Received: 10 April 2018 Accepted: 11 July 2018

Published online: 06 August 2018

References

- Chen, C. T. et al. Design and synthesis of an ultraviolet-transparent nonlinear optical crystal. $Sr_2Be_2B_2O_7$. *Nature* **373**, 322–324 (1995).
- Puggionil, D. & James, M. R. Designing a robustly metallic noncentrosymmetric ruthenate oxide with large thermopower anisotropy. *Nat. Commun.* **5**, 3432 (2014).
- Chung, I. & Mercouri, G. K. Metal chalcogenides: a rich source of nonlinear optical materials. *Chem. Mater.* **26**, 849–869 (2014).
- Wu, K., Yang, Z. H. & Pan, S. L. The first quaternary diamond-like semiconductor with 10-membered Li_4 rings exhibiting excellent nonlinear optical performances. *Chem. Commun.* **53**, 3010–3013 (2017).
- Sasaki, T., Mori, Y., Yoshimura, M., Yap, Y. K. & Kamimura, T. Recent development of nonlinear optical borate crystals: key materials for generation of visible and UV light. *Mater. Sci. Eng. R.* **30**, 1–54 (2000).
- Jiang, X. X. et al. First-principles evaluation of the alkali and/or alkaline earth beryllium borates in deep ultraviolet nonlinear optical applications. *ACS Photonics* **2**, 1183–1191 (2015).
- Ok, K. M. Toward the rational design of novel non-centrosymmetric materials: factors influencing the framework structures. *Acc. Chem. Res.* **49**, 2774–2785 (2016).
- Zou, G. H. et al. Pb_2BO_3Cl : a tailor-made polar lead borate chloride with very strong second harmonic generation. *Angew. Chem. Int. Ed.* **55**, 12078–12082 (2016).
- Aka, G. et al. Linear- and nonlinear-optical properties of a new gadolinium calcium oxoborate crystal, $Ca_4GdO(BO_3)_3$. *J. Opt. Soc. Am. B* **14**, 2238–2247 (1997).
- Chen, C. T. et al. *Nonlinear Optical Borate Crystals: Principles and Applications* (Wiley-VCH, Weinheim, 2012).
- Li, L. Y., Li, G. B., Wang, Y. X., Liao, F. H. & Lin, J. H. Bismuth borates: one-dimensional borate chains and nonlinear optical properties. *Chem. Mater.* **17**, 4174–4180 (2005).
- Wei, Q., Wang, J. J., He, C., Cheng, J. W. & Yang, G. Y. Deep-ultraviolet nonlinear optics in a borate framework with 21-ring channels. *Chem. Eur. J.* **31**, 10759–10762 (2016).
- Kong, F., Huang, S. P., Sun, Z. M., Mao, J. G. & Cheng, W. D. A new type of second-order NLO material. *J. Am. Chem. Soc.* **128**, 7750–7751 (2006).
- Song, J. L., Hu, C. L., Xu, X., Kong, F. & Mao, J. G. A facile synthetic route to a new SHG material with two types of parallel π -conjugated planar triangular units. *Angew. Chem. Int. Ed.* **54**, 3679–3682 (2015).
- Huppertz, H. & von der Eltz, B. Multianvil high-pressure synthesis of $Dy_4B_6O_{15}$: the first oxoborate with edge-sharing BO_4 tetrahedra. *J. Am. Chem. Soc.* **124**, 9376–9377 (2002).
- Sohr, G. et al. High-pressure synthesis of $Cd(NH_3)_2[B_3O_5(NH_3)_2]$ way to the substance class of ammine borates. *Angew. Chem. Int. Ed.* **54**, 6360–6363 (2015).
- Dadachov, M. S., Sun, K., Conradsson, T. & Zou, X. D. The first templated borogermanate $(C_2N_2H_{10})_2[(BO_{2.5})_2(GeO_2)_3]$: linkage of tetrahedra of significantly different sizes. *Angew. Chem. Int. Ed.* **39**, 3674–3676 (2000).
- Guo, P. et al. Accurate structure determination of a borosilicate zeolite EMM-26 with two-dimensional 10×10 ring channels using rotation electron diffraction. *Inorg. Chem. Front.* **3**, 1444–1448 (2016).
- Chen, C. T., Wang, G. L., Wang, X. Y. & Xu, Z. Y. Deep-UV nonlinear optical crystal $KBe_2BO_3F_2$ -discovery, growth, optical properties and applications. *Appl. Phys. B: Lasers Opt.* **97**, 9–25 (2009).
- Hu, Z. G., Yoshimura, M., Mori, Y. & Sasaki, T. Growth of a new nonlinear optical crystal $BaAlBO_3F_2$. *J. Cryst. Growth* **260**, 287–290 (2004).
- Huang, H. W. et al. $NaSr_3Be_3B_3O_9F_4$: A promising deep-ultraviolet nonlinear optical material resulting from the cooperative alignment of the $[Be_3B_3O_{12}F]^{10-}$ anionic group. *Angew. Chem. Int. Ed.* **50**, 9141–9144 (2011).
- Zhao, S. G. et al. Beryllium-free $Li_4Sr(BO_3)_2$ for deep-ultraviolet nonlinear optical applications. *Nat. Commun.* **5**, 4019 (2014).
- McMillen, C. D., Stritzinger, J. T. & Kolis, J. W. Two novel acentric borate fluorides: $M_3B_6O_{11}F_2$ ($M = Sr, Ba$). *Inorg. Chem.* **51**, 3953–3855 (2012).
- Rashchenko, S. V. et al. New fluoride borate solid–solution series $Ba_{4-x}Sr_3+x(BO_3)_{4-y}F_{2+3y}$. *Cryst. Growth Des.* **12**, 2955–2960 (2012).
- Bekker, T. B., Vedenyapin, V. N. & Khamoyan, A. G. Birefringence of the new fluoride borates $Ba_2Na_3[B_3O_6]_2F$ and $Ba_7(BO_3)_{4-y}F_{2+3y}$ in the Na, Ba, B/O, F quaternary reciprocal system. *Mater. Res. Bull.* **91**, 54–58 (2017).
- Shi, G. Q. et al. Finding the next deep-ultraviolet nonlinear optical material: $NH_4B_4O_6F$. *J. Am. Chem. Soc.* **139**, 10645–10648 (2017).
- Mutailipu, M. et al. $SrB_5O_7F_3$ functionalized with $[B_5O_9F_3]^{6-}$ chromophores: accelerating the rational design of deep-ultraviolet nonlinear optical materials. *Angew. Chem. Int. Ed.* **57**, 6095–6099 (2018).
- Pilz, T. & Jansen, M. $Li_2B_6O_9F_2$, a new acentric fluorooxoborate. *Z. Anorg. Allg. Chem.* **637**, 2148–2152 (2011).
- Jantz, S. G. et al. The first alkaline-earth fluorooxoborate $Ba[B_4O_6F_2]$ -characterisation and doping with Eu^{2+} . *Chem. Eur. J.* **24**, 443–450 (2018).
- Zhang, H. et al. $Na_3Ba_2(B_3O_6)_2F$: next generation of deep-ultraviolet birefringent materials. *Cryst. Growth Des.* **15**, 523–259 (2015).
- Becker, P. Borate materials in nonlinear optics. *Adv. Mater.* **10**, 979–992 (1998).
- Xia, Z. G. & Poepplmeier, K. R. Chemistry-inspired adaptable framework structures. *Acc. Chem. Res.* **50**, 1222–1230 (2017).
- Mutailipu, M. et al. Chemical cosubstitution-oriented design of rare-earth borates as potential ultraviolet nonlinear optical materials. *J. Am. Chem. Soc.* **139**, 18397–18405 (2017).
- Li, R. K. & Chen, P. Cation coordination control of anionic group alignment to maximize SHG effects in the $BaMBO_3F$ ($M = Zn, Mg$) series. *Inorg. Chem.* **49**, 1561–1565 (2010).
- Luo, M., Ye, N., Zou, G. H., Lin, C. S. & Cheng, W. D. $Na_8Lu_2(CO_3)_6F_2$ and $Na_3Lu(CO_3)_2F_2$: rare earth fluoride carbonates as deep-UV nonlinear optical materials. *Chem. Mater.* **25**, 3147–3153 (2013).
- Tran, T. T., He, J. G., Rondinelli, J. M. & Halasyamani, P. S. $RbMgCO_3F$: A new beryllium-free deep-ultraviolet nonlinear optical material. *J. Am. Chem. Soc.* **137**, 10504–10507 (2015).
- Huang, H. W. et al. Deep-ultraviolet nonlinear optical materials: $Na_2Be_4B_4O_{11}$ and $LiNa_5Be_{12}B_{12}O_{33}$. *J. Am. Chem. Soc.* **135**, 18319–18322 (2013).
- Zhao, S. G. et al. A new UV nonlinear optical material $CsZn_2B_3O_7 \cdot ZnO_4$ tetrahedra double the efficiency of second-harmonic generation. *Inorg. Chem.* **53**, 2521–2527 (2014).
- Yu, H. W. et al. $Cs_3Zn_6B_9O_{21}$: A chemically benign member of the KBBF family exhibiting the largest second harmonic generation response. *J. Am. Chem. Soc.* **136**, 1264–1267 (2014).
- Chen, C. T., Wu, B. C., Jiang, A. D. & You, G. M. A new type ultraviolet SHG crystal: β - BaB_2O_4 . *Sci. Sin. B* **28**, 235–243 (1985).
- Kurtz, S. K. & Perry, T. T. A powder technique for the evaluation of nonlinear optical materials. *J. Appl. Phys.* **39**, 3798–3813 (1968).
- Lee, M. H., Yang, C. H. & Jan, J. H. Band-resolved analysis of nonlinear optical properties of crystalline and molecular materials. *Phys. Rev. B* **70**, 235110 (2004).
- Krukau, A. V., Vydrov, O. A., Izmaylov, A. F. & Scuseria, G. E. Influence of the exchange screening parameter on the performance of screened hybrid functionals. *J. Chem. Phys.* **125**, 224106 (2006).

44. Kohn, W. & Sham, L. J. Self-consistent equations including exchange and correlation effects. *Phys. Rev.* **140**, A1133–A1138 (1965).
45. SAINT version 7.60A (Bruker analytical X-ray instruments, Inc., 2008).
46. Sheldrick, G. M. A short history of SHELX. *Acta Crystallogr. A* **64**, 112–122 (2008).
47. Spek, A. L. Single-crystal structure validation with the program PLATON. *J. Appl. Crystallogr.* **36**, 7–13 (2003).
48. Clark, S. J. et al. First principles methods using CASTEP. *Z. Anorg. Allg. Chem.* **220**, 567–570 (2005).
49. Blaha, P., Schwarz, K., Madsen, G., Kvaniscka, D. & Luitz, J. *Wien2k* (Vienna University of Technology, Vienna, Austria, 2001).
50. Rappe, A. M., Rabe, K. M., Kaxiras, E. & Joannopoulos, J. D. Optimized pseudopotentials. *Phys. Rev. B* **41**, 1227 (1990).

Acknowledgements

This work was financially supported by National Natural Science Foundation of China (Grant Nos. 21501194, 51425206, 51602341, and 91622107), the National Key Research Project (Grant Nos. 2016YFB1102302 and 2016YFB0402104), Xinjiang Key Research and Development Program (Grant No. 2016B02021), National Basic Research Program of China (Grant No. 2014CB648400), and West Light Foundation of the Chinese Academy of Sciences (Grant No. 2016-YJRC-2).

Author contributions

M.M. and M.Z. grew the single crystals and performed the experiments, data analysis, and paper writing. H.W. supervised the optical experiments. Z.Y. developed the theoretical calculations. Y.S. performed the crystal data collection. J.S. and S.P. designed and supervised the experiments. All the authors discussed the results and commented on the manuscript.

Additional information

Supplementary Information accompanies this paper at <https://doi.org/10.1038/s41467-018-05575-w>.

Competing interests: The authors declare no competing interests.

Reprints and permission information is available online at <http://npg.nature.com/reprintsandpermissions/>

Publisher's note: Springer Nature remains neutral with regard to jurisdictional claims in published maps and institutional affiliations.



Open Access This article is licensed under a Creative Commons Attribution 4.0 International License, which permits use, sharing, adaptation, distribution and reproduction in any medium or format, as long as you give appropriate credit to the original author(s) and the source, provide a link to the Creative Commons license, and indicate if changes were made. The images or other third party material in this article are included in the article's Creative Commons license, unless indicated otherwise in a credit line to the material. If material is not included in the article's Creative Commons license and your intended use is not permitted by statutory regulation or exceeds the permitted use, you will need to obtain permission directly from the copyright holder. To view a copy of this license, visit <http://creativecommons.org/licenses/by/4.0/>.

© The Author(s) 2018